




Cite this: *RSC Adv.*, 2022, 12, 15020

A uniformly anchored zirconocene complex on magnetic reduced graphene oxide (rGO@Fe₃O₄/ZrCp₂Cl_x (x = 0, 1, 2)) as a novel and reusable nanocatalyst for synthesis of *N*-arylacetamides and reductive-acetylation of nitroarenes†

Massood Bayzidi  and Behzad Zeynizadeh *

In this study, a crafted zirconocene complex on rGO@Fe₃O₄ as a novel magnetic nanocatalyst was synthesized and then characterized using FT-IR, SEM, EDX, VSM, ICP-OES, TGA, BET and MS analyses. Next, catalytic activity of the prepared nanocomposite rGO@Fe₃O₄/ZrCp₂Cl_x (x = 0, 1, 2) towards successful reduction of aromatic nitro compounds to arylamines using N₂H₄·H₂O (80%) was investigated. The examined nanocatalyst also showed perfect catalytic activity for reductive-acetylation of aromatic nitro compounds to the corresponding *N*-arylacetamides without isolation of the prepared *in situ* amines using the N₂H₄·H₂O/Ac₂O system. Furthermore, acetylation of the commercially available arylamines to the corresponding *N*-arylacetamides was carried out by acetic anhydride in the presence of the rGO@Fe₃O₄/ZrCp₂Cl_x (x = 0, 1, 2) nanocomposite. All reactions were carried out in refluxing EtOH as a green solvent to afford the products in high yields. The obtained results exhibited that the nanocomposite of rGO@Fe₃O₄/ZrCp₂Cl_x (x = 0, 1, 2) showed a great catalytic activity in comparison to rGO and rGO@Fe₃O₄ as the parent constituents. Recovery and reusability of rGO@Fe₃O₄/ZrCp₂Cl_x (x = 0, 1, 2) were also examined for 8 consecutive cycles without significant loss of the catalytic activity. This establishes the sustainable anchoring of the zirconocene complex on the surface and mesopores of the rGO@Fe₃O₄ nanohybrid system.

Received 8th April 2022

Accepted 9th May 2022

DOI: 10.1039/d2ra02293a

rsc.li/rsc-advances

Introduction

In recent years zirconium complexes have played a key role as catalysts or reagents in organic synthesis.¹ One of the first examples of the use of zirconium as a catalyst was zirconocene complexes in Ziegler–Natta polymerization.² Schwartz reagent as a hydrozirconation and reducing agent was the second application of zirconocene complexes.³ In *in situ* generation of the Schwartz reagent for hydrozirconation and reduction reactions, the use of different hydride sources such as LiAlH₄, NaAlH₂(OCH₂CH₂OCH₃)₂ (Red-Al),⁴ t-BuMgCl,⁵ LiEt₃BH⁶ and DIBAL-H⁷ has also been reported. In this context, using hydrazine hydrate as a commercially available hydrogen source could be convenient due to green by-products of N₂ gas and water.⁸

To overcome problems related to the separation and reusability of the homogeneous catalyst systems, using magnetic nanoparticles are one of the prominent candidates.^{9,10} Magnetic

nanoparticles can be easily separated from the reaction medium using an external magnetic field, no need to filtration, centrifugation or other tedious workup procedures.¹¹ Over the last few years, magnetic cores as well as their coating surfaces have dramatically improved and widely used for different purposes. These improvements have been made in order to increase the accessible sites/zones on the surface of catalyst, greater catalyst reactivity and selectivity, thermal stability and finally easy separation. Fe₃O₄,^{12,13} NiFe₂O₄,^{14–16} CoFe₂O₄,¹⁷ CuFe₂O₄,^{18–20} MnFe₂O₄,²¹ Ni–Cu–ZnFe₂O₄,²² BiFeO₃,²³ FeAl₂O₄,²⁴ and ZnCrFeO₄,²⁵ as a core, and metals,^{26–28} silica,^{29–32} polymers,^{33–35} carbon nanotubes and sheets,^{36–40} cellulose,⁴¹ small organic molecules,^{42,43} ionic liquids,^{44,45} and organosulfonic acids^{46,47} have been used as a coating.

Recently, the magnetic hybrid composites were prepared by the combination of reduced graphene oxide (rGO) and magnetic materials. Among the hybrid composite systems, rGO@Fe₃O₄ is highly regarded for its low price, excellent magnetic property, easy preparation method, high biocompatibility and low toxicity.⁴⁸ Generally, reduced graphene oxide sheets (rGO) can be easily prepared by oxidative exfoliation of graphite flakes in a large scale followed by chemically or thermally reduction.⁴⁹ Due to unique electronic and structural properties such as high

Department of Chemistry, Urmia University, Urmia 5756151818, Iran. E-mail: m.bayzidi@urmia.ac.ir; massoodbayzidi@gmail.com; b.zeynizadeh@urmia.ac.ir; bzeynizadeh@gmail.com

† Electronic supplementary information (ESI) available. See <https://doi.org/10.1039/d2ra02293a>



intrinsic carrier mobility, high mechanical strength and thermal stability, rGO and rGO-based materials have attracted a great deal of attention. Because of the advantages including 2D structure character as well as the large surface area, surface defects and the aromatic scaffold, rGO can also serve as a potential support for the fabrication of hybrid nano-materials.^{50–56} Moreover, electronic properties including charge transfer, magnetism, band structure, and density of states are closely interrelated with the metal-support interaction. Charge transfer occurs between the adsorbed/embedded metal and rGO supports due to their different Fermi levels.^{57,58} In this context, the present study clearly represents that when zirconium as the form of zirconocene is immobilized on the surface and mesopores of magnetite-reduced graphene oxide, the prepared $\text{rGO@Fe}_3\text{O}_4/\text{ZrCp}_2\text{Cl}_x$ ($x = 0, 1, 2$) nanohybrid system, due to the facilitated electronic transfer between zirconocene and rGO constituents, was able to perform organic reactions more easily.

On the other hand, aromatic amines are critical starting materials and intermediates for synthesis of various chemicals such as medicines, biomaterials, dyes, agricultural materials and so on.⁵⁹ One simple and straightforward method for the preparation of aromatic amines is the catalytic reduction of nitroarene compounds by various reducing systems.⁶⁰ In this context, heterogenization of metal catalysts through the immobilization of transition metals species on solid supporters is the widely used strategy in organic synthesis.^{61–68}

Furthermore, the catalytic formation of amide bonds is one of the most intended procedures in the synthesis of various organic compounds including polymers, agrochemicals, pharmaceuticals and fragrances.⁶⁹ Due this, acetylation of arylamines and reductive-acetylation of aromatic nitro compounds by acetic anhydride are the commonly used strategies for the preparation of *N*-arylamides. The literature review shows

that although the application of transition metals (Mn, Co, Ni, Cu and Zn) based catalyst systems have been reported for the titled transformations,^{63,68,70,71} however, using any zirconium species did not yet reported in this area.

In line with the outlined strategies and continuation of our research programs towards reduction of aromatic nitro compounds to arylamines and acetylation of arylamines to *N*-arylamides in the presence of transition metals-based nanocatalyst systems,^{72–77} herein, we report the synthesis of a novel nanohybrid material by the immobilization of zirconocene on magnetic reduced graphene oxide. The prepared $\text{rGO@Fe}_3\text{O}_4/\text{ZrCp}_2\text{Cl}_x$ ($x = 0, 1, 2$) nanocomposite was then characterized and its catalytic activity was successfully studied towards reduction and reductive-acetylation of nitroarenes as well as *N*-acetylation of the commercially available anilines in refluxing ethanol as a green solvent.

Results and discussion

Catalyst characterization

The study was started by the synthesis of $\text{rGO@Fe}_3\text{O}_4/\text{ZrCp}_2\text{Cl}_x$ ($x = 0, 1, 2$) nanocomposite in a four-step procedure as shown in Fig. 1. This is a general synthetic approach and the details are described in the Experimental section. Primarily graphite flakes were oxidized by H_2SO_4 and KMnO_4 to afford graphene oxide (GO) followed by the reduction with L-ascorbic acid to afford exfoliated reduced graphene oxide (rGO). Next, through the mixing of an aqueous solution of $\text{FeCl}_3 \cdot 6\text{H}_2\text{O}$ and $\text{FeCl}_2 \cdot 4\text{H}_2\text{O}$ with the prepared rGO and then dropwise addition of an aqueous solution of ammonia 25% under N_2 atmosphere, the magnetic reduced graphene oxide ($\text{rGO@Fe}_3\text{O}_4$) was prepared. Finally, refluxing the benzene solution of ZrCp_2Cl_2 with nanoparticles of magnetic rGO affords $\text{rGO@Fe}_3\text{O}_4/\text{ZrCp}_2\text{Cl}_x$ ($x = 0, 1,$

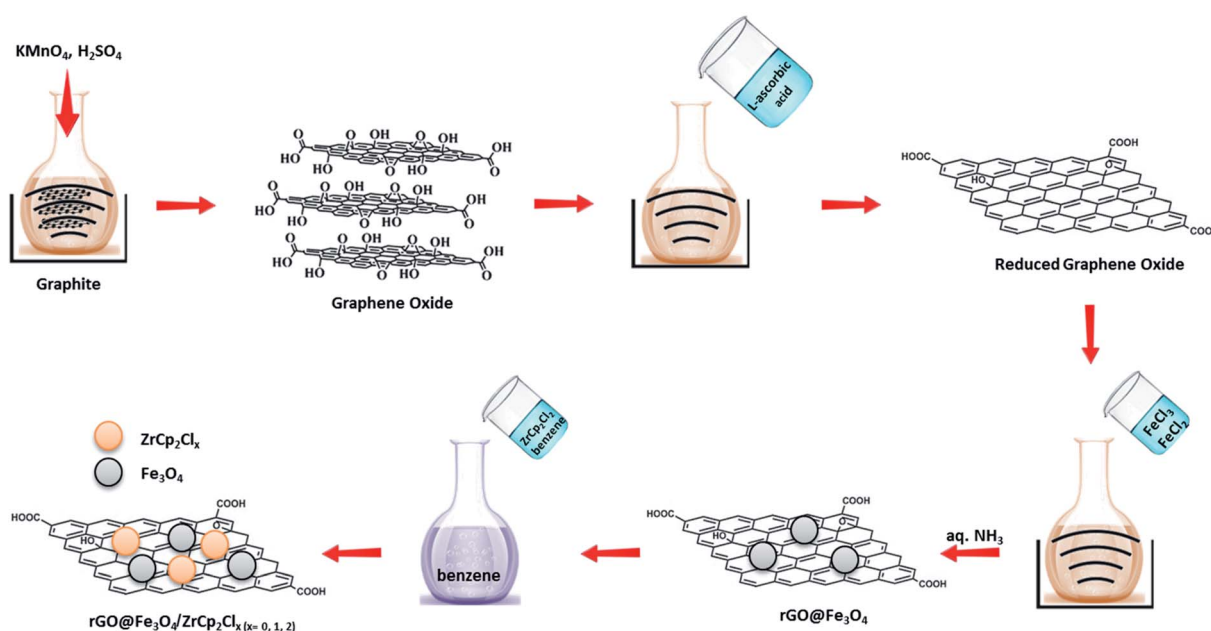


Fig. 1 Synthesis of $\text{rGO@Fe}_3\text{O}_4/\text{ZrCp}_2\text{Cl}_x$ ($x = 0, 1, 2$) nanohybrid material.

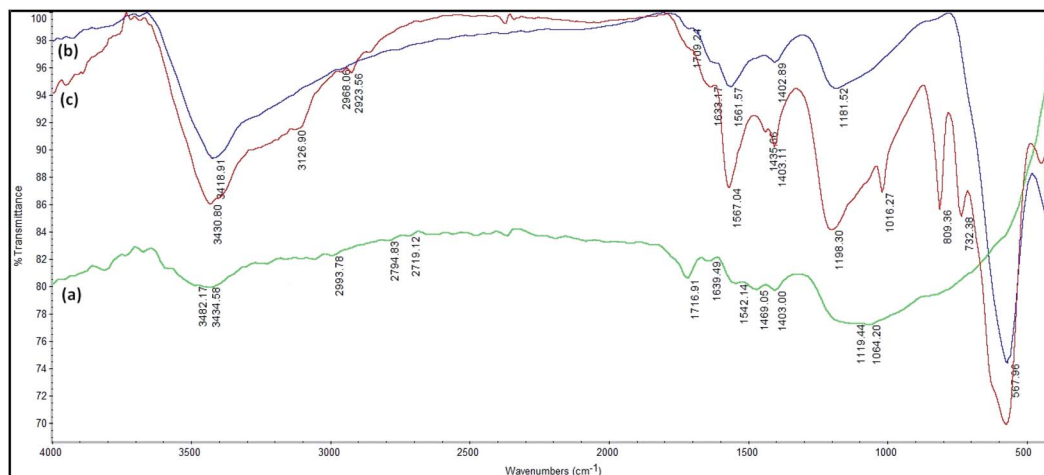


Fig. 2 FT-IR spectra of (a) rGO, (b) rGO@Fe₃O₄ and (c) rGO@Fe₃O₄/ZrCp₂Cl_x ($x = 0, 1, 2$) composite systems.

2) nanohybrid material. The prepared nanocatalyst system was then characterized using FT-IR, SEM, EDX, VSM, ICP-OES, TGA, BET and MS analyses.

FT-IR spectra of rGO, rGO@Fe₃O₄ and rGO@Fe₃O₄/ZrCp₂Cl_x ($x = 0, 1, 2$) composite systems are shown in Fig. 2. In FT-IR spectrum of rGO (Fig. 2a), the broad band around 3300–3650 cm⁻¹ shows the stretching vibration of O–H groups due to the presence of adsorbed water and carboxyl and hydroxyl functionalities. The bands at 2993 cm⁻¹ and 1716 cm⁻¹ are also attributed to asymmetric/symmetric vibrations of CH₂ and stretching vibration of C=O groups, respectively.⁷⁸ As well the broad band around 850–1250 cm⁻¹ shows the bending vibrations of C–O–C and O–H groups. In addition to the all bond frequencies of rGO, the stretching vibration of Fe–O is appeared at 580 cm⁻¹ in FT-IR spectrum of rGO@Fe₃O₄ (Fig. 2b). In FT-IR spectrum of rGO@Fe₃O₄/ZrCp₂Cl_x ($x = 0, 1, 2$) (Fig. 2c), the absorption peak at 1567 cm⁻¹ is attributed to the stretching vibration of C=C group due to existence of Cp groups and aromatic constituents in the structure of rGO. The weak peak at 1633 cm⁻¹ is assigned to the stretching and bending vibrations of OH groups due to the adsorbed water on the surface of rGO. The peak observed at 1403 cm⁻¹ is attributed to C–O–H deforming vibration. The broad band around 1198 cm⁻¹ is corresponded to C–O–C and C–O stretching vibrations. In addition, the peaks at 732, 809 and 1016 cm⁻¹ are accordance with zirconocene dichloride spectrum. All these are indicated that ZrCp₂Cl_x species were successfully anchored on the mesopores and surface of rGO@Fe₃O₄ constituents.

Structural elucidation of rGO, rGO@Fe₃O₄ and rGO@Fe₃O₄/ZrCp₂Cl_x ($x = 0, 1, 2$) composite systems was also carried out using X-ray diffraction (XRD) analysis (Fig. 3). In this context, the existence of individual sharp peaks in the depicted XRD patterns represents that all the examined composite systems have the extent of crystallinity character. In this context, the XRD pattern of Fe₃O₄ (Fig. 3a) shows that the diffraction peaks at $2\theta = 30.2^\circ, 35.5^\circ, 43.3^\circ, 53.7^\circ, 57.2^\circ$ and 62.9° are attributed to (2 2 0), (3 1 1), (4 0 0), (4 2 2), (5 1 1) and (4 4 0) crystal planes of nano Fe₃O₄. The laboratory sample of nano Fe₃O₄ has

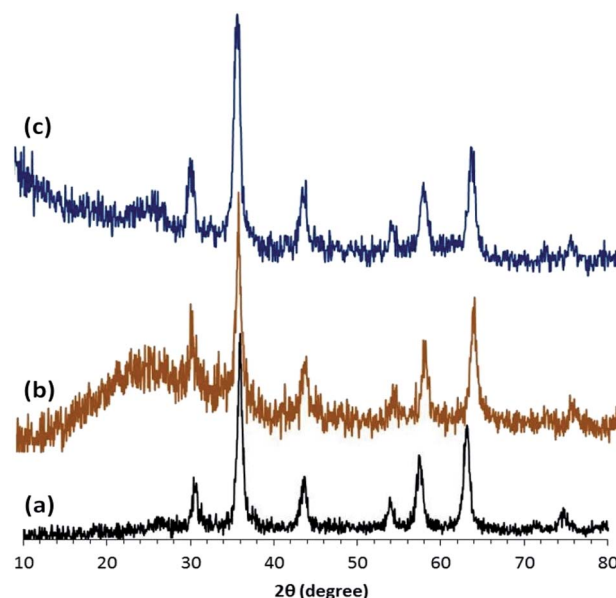


Fig. 3 XRD patterns of (a) Fe₃O₄, (b) rGO@Fe₃O₄ and (c) rGO@Fe₃O₄/ZrCp₂Cl_x ($x = 0, 1, 2$).

a crystalline cubic spinel structure and it is in agreement with the standard one of JCPDS 65-3107. As well, the XRD pattern of rGO@Fe₃O₄ represents that besides to the all diffraction peaks of nano Fe₃O₄, the position of a broad peak at $2\theta = 16\text{--}28^\circ$ is attributed to rGO constituents. Fig. 3c also shows that the XRD pattern of rGO@Fe₃O₄/ZrCp₂Cl_x ($x = 0, 1, 2$) is similar to that of Fe₃O₄ and rGO@Fe₃O₄. This similarity could be attributed to low loading of Zr and due this the diffraction peaks for zirconium species have very low intensity or overlap with the peaks of Fe₃O₄.

Scanning electron microscopy (SEM) was used to study the morphology and size distribution of rGO, rGO@Fe₃O₄ and rGO@Fe₃O₄/ZrCp₂Cl_x ($x = 0, 1, 2$) composite systems (Fig. 4). Analysis of the images shows that the immobilization of Fe₃O₄ MNPs (magnetic nanoparticles) and ZrCp₂Cl_x species on rGO



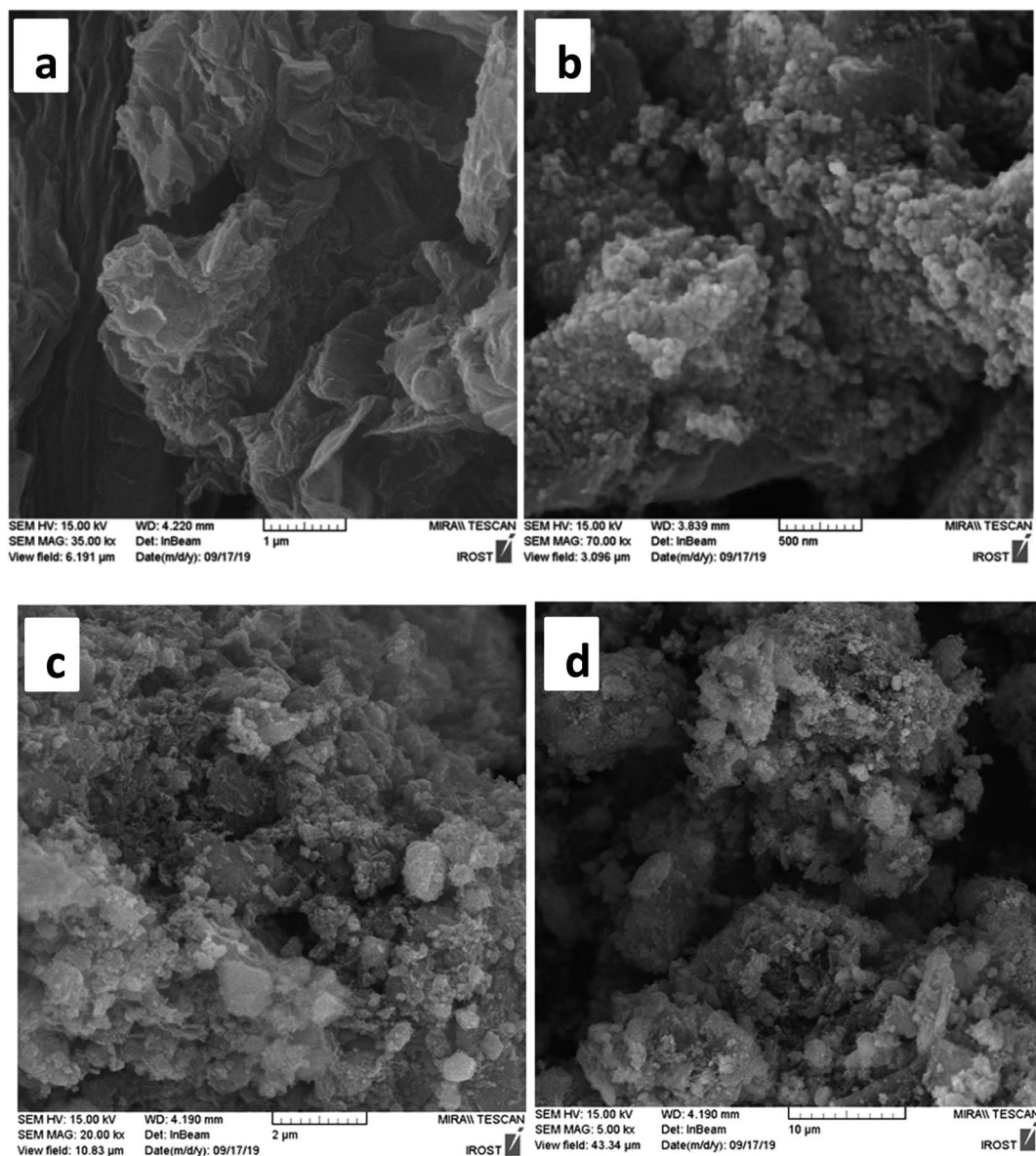


Fig. 4 SEM images of (a) rGO, (b) rGO@Fe₃O₄, (c and d) rGO@Fe₃O₄/ZrCp₂Cl_x ($x = 0, 1, 2$).

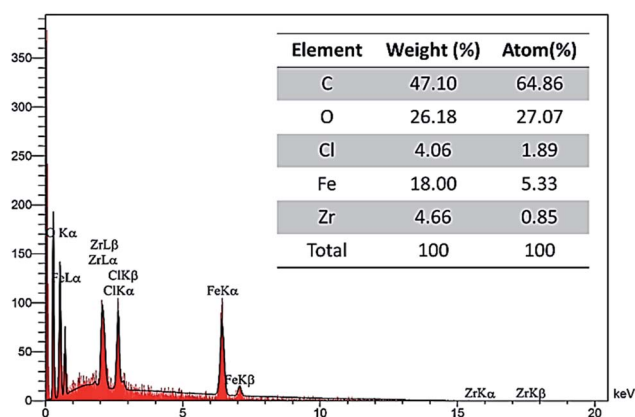


Fig. 5 EDX analysis of rGO@Fe₃O₄/ZrCp₂Cl_x ($x = 0, 1, 2$).

are successful. In this context, Fig. 4a reveals that rGO constituents have the wrinkled and folded morphology, and so this causes the well distribution of Fe₃O₄ and ZrCp₂Cl_x species on rGO. In addition, the mentioned morphology prevents accumulation and agglomeration of Fe₃O₄ and ZrCp₂Cl_x species in the composition of rGO. The average particle size of rGO@Fe₃O₄ and rGO@Fe₃O₄/ZrCp₂Cl_x are to be 25 and 80 nm, respectively.

Elemental elucidation of the synthesized rGO@Fe₃O₄/ZrCp₂Cl_x ($x = 0, 1, 2$) nanohybrid material was carried out using energy-dispersive X-ray spectroscopy (EDX) (Fig. 5). The analysis shows that all the required elements including C (47.10%), O (26.18%), Cl (4.06%), Fe (18.00%) and Zr (4.66%) are present in the structure of rGO@Fe₃O₄/ZrCp₂Cl_x system. In addition, distribution of the elements was investigated using EDX-mapping analysis (Fig. 6). The mapping for Fe, C and Zr elements shows that they were uniformly distributed in all

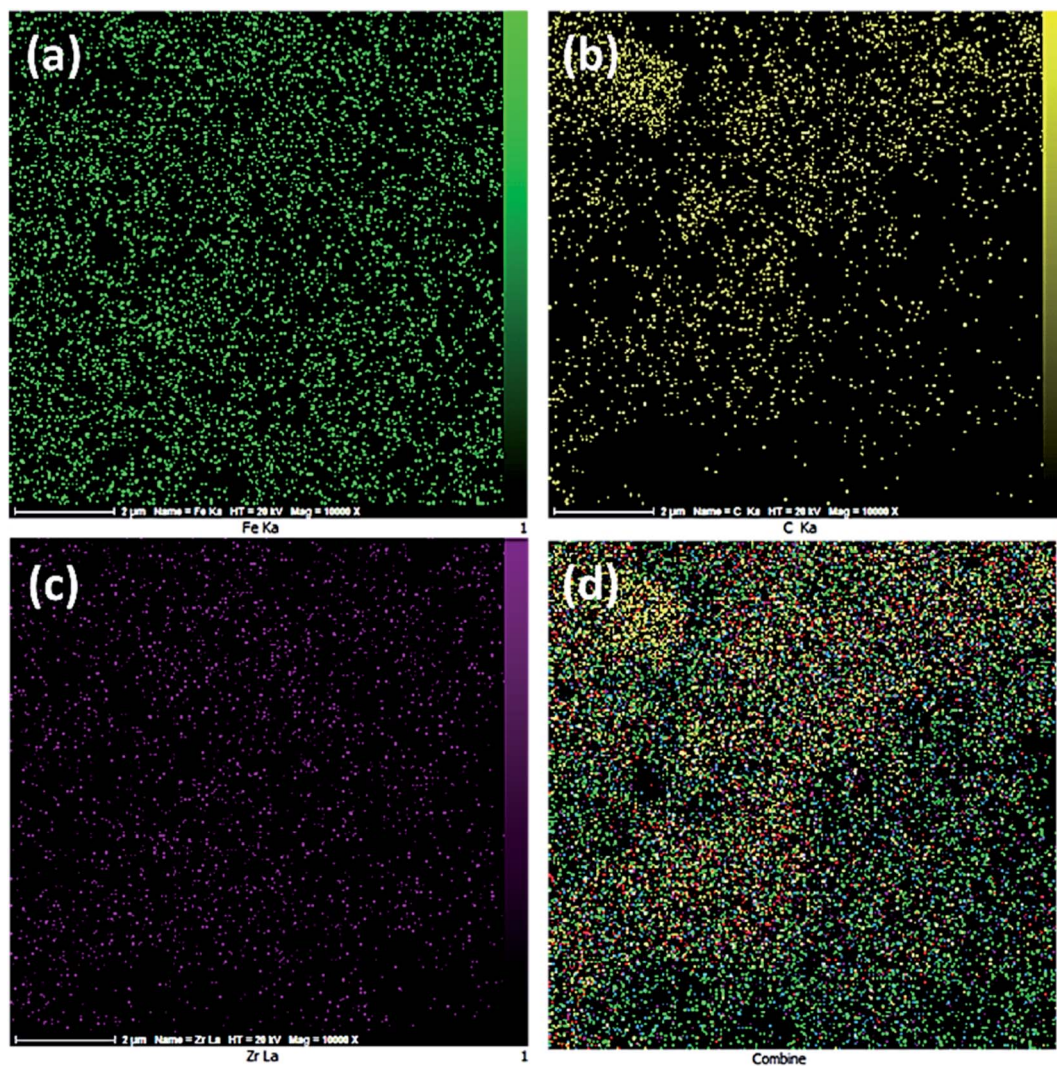


Fig. 6 Elemental mapping of (a) Fe, (b) C, (c) Zr and (d) Fe, C, and Zr in $\text{rGO@Fe}_3\text{O}_4/\text{ZrCp}_2\text{Cl}_x$ ($x = 0, 1, 2$).

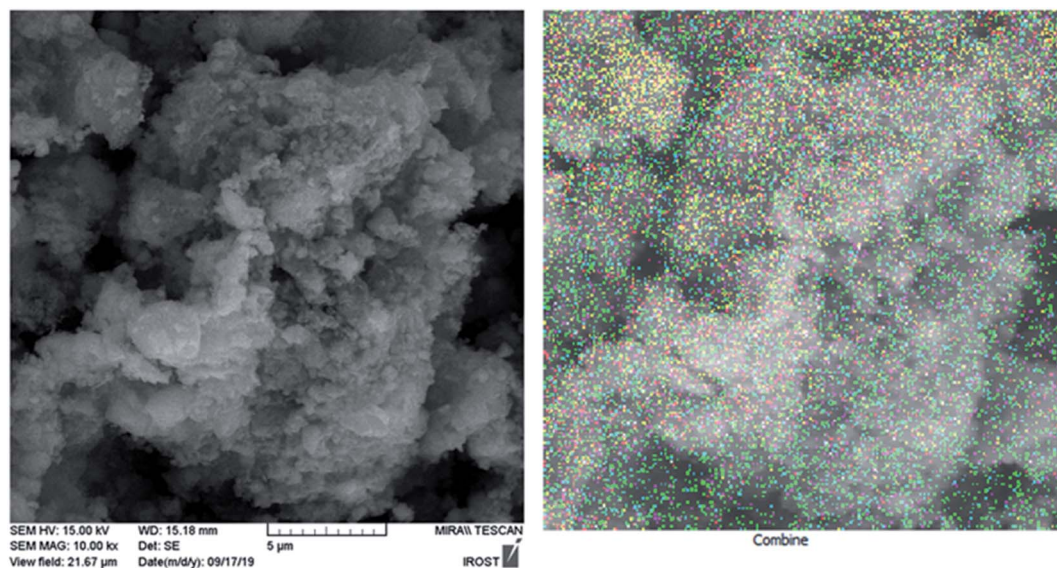


Fig. 7 SEM image and its EDX-elemental mapping analyses of $\text{rGO@Fe}_3\text{O}_4/\text{ZrCp}_2\text{Cl}_x$ ($x = 0, 1, 2$).



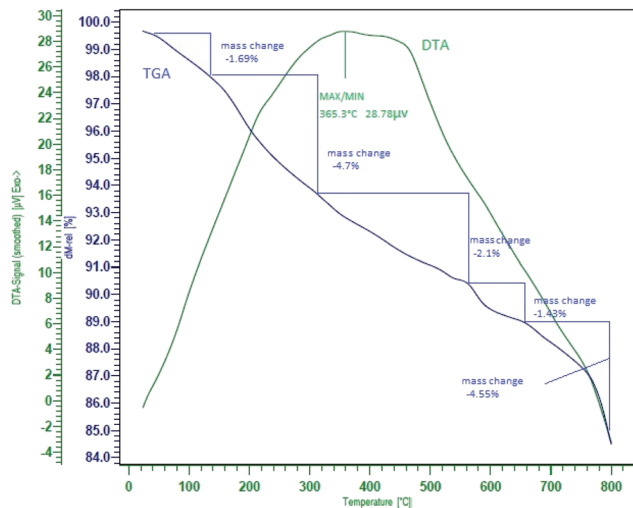


Fig. 8 TGA and DTA analysis of $\text{rGO@Fe}_3\text{O}_4/\text{ZrCp}_2\text{Cl}_x$ ($x = 0, 1, 2$).

around of $\text{rGO@Fe}_3\text{O}_4/\text{ZrCp}_2\text{Cl}_x$ composite system. SEM and elemental mapping analysis of $\text{rGO@Fe}_3\text{O}_4/\text{ZrCp}_2\text{Cl}_x$ were carried out through the depicted image in Fig. 7.

Based on the ICP-OES (inductively coupled plasma optical emission spectrometry), the exact amount of Zr in $\text{rGO@Fe}_3\text{O}_4/\text{ZrCp}_2\text{Cl}_x$ composite system is 4.7%. The measure is exactly in accordance with the obtained data through the EDX-elemental analysis of zirconium (Fig. 5).

Thermogravimetric analysis (TGA) of $\text{rGO@Fe}_3\text{O}_4/\text{ZrCp}_2\text{Cl}_x$ nanohybrid material was used to study the stability and weight loss of the immobilized zirconocene on $\text{rGO@Fe}_3\text{O}_4$ (Fig. 8). The depicted curve represents that 1.69% weight loss in the area of 40–150 °C is attributed to the evaporation of adsorbed water on the surface of $\text{rGO@Fe}_3\text{O}_4/\text{ZrCp}_2\text{Cl}_x$ composite system. As well, the weight loss of 4.7% in the range of 150–320 °C indicates removing of organic moieties such as Cp from the immobilized ZrCp_2Cl_x and RCO_2H , RCOR , ROR or ROH species from the rGO constituents. The third weight loss of 3.53% at the area of 350–800 °C is attributed to the fragmentation and

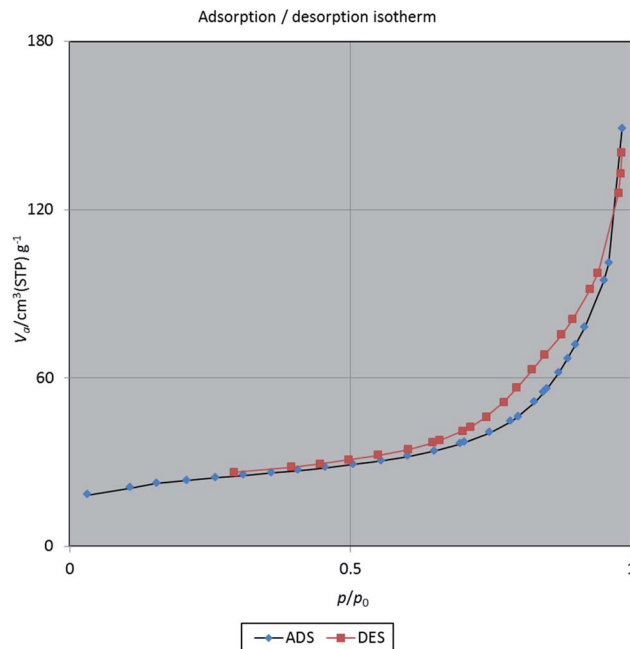


Fig. 10 N_2 adsorption–desorption isotherm of $\text{rGO@Fe}_3\text{O}_4/\text{ZrCp}_2\text{Cl}_x$ ($x = 0, 1, 2$).

decomposition of the composite system. Differential thermal analysis (DTA) clearly shows that the examined nanocomposite has a good thermal stability up to 365 °C with weight loss of 6.39%.

Characterization of $\text{rGO@Fe}_3\text{O}_4/\text{ZrCp}_2\text{Cl}_x$ ($x = 0, 1, 2$) system was also carried out using mass spectroscopy at the ionization potential of 20 eV. The depicted graph in Fig. 9 shows the fragmentation pattern of the anchored zirconocene on $\text{rGO@Fe}_3\text{O}_4$. In this context, the presence of fragments in $m/z = 56 \pm 1$ [Fe], 65 [Cp], 72 [FeO], 91 [Zr], 160 [Fe₂O₃], 192 [ZrCpCl], 221–2 [ZrCp₂] and 292 [ZrCp₂Cl₂] exactly confirms the immobilization of ZrCp_2Cl_x species on $\text{rGO@Fe}_3\text{O}_4$ constituents.

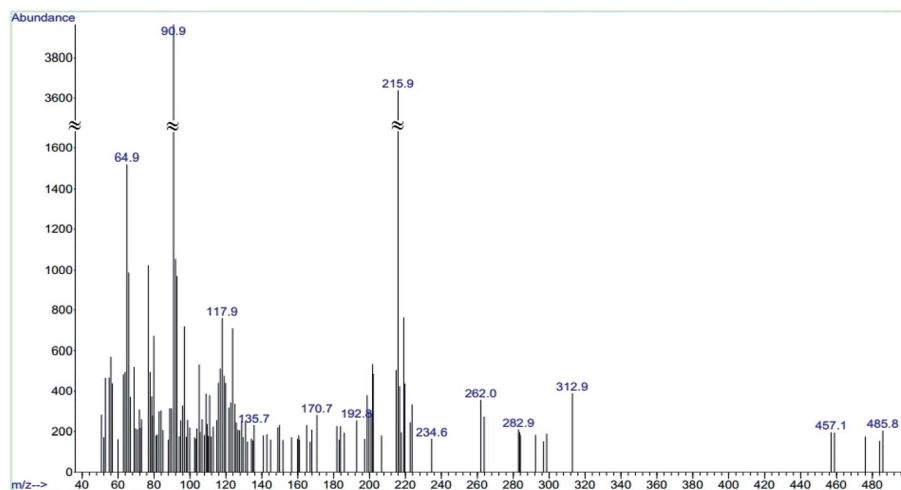


Fig. 9 Mass spectrum of $\text{rGO@Fe}_3\text{O}_4/\text{ZrCp}_2\text{Cl}_x$ ($x = 0, 1, 2$) at 20 eV ionization potential.

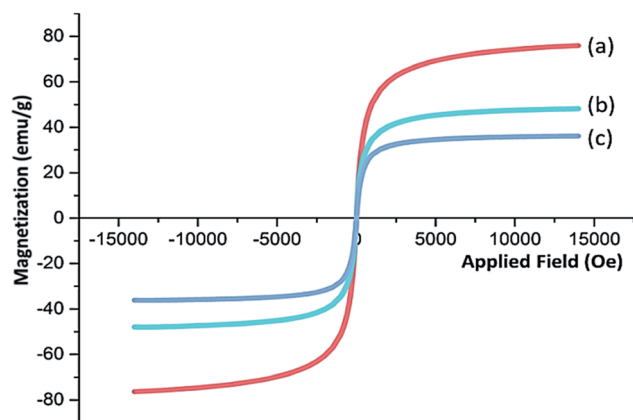


Fig. 11 Magnetization curve of (a) Fe_3O_4 , (b) $\text{rGO@Fe}_3\text{O}_4$ and (c) $\text{rGO@Fe}_3\text{O}_4/\text{ZrCp}_2\text{Cl}_x$ ($x = 0, 1, 2$).

N_2 adsorption-desorption analysis is further utilized to determine specific surface area and porosity of the surface in $\text{rGO@Fe}_3\text{O}_4/\text{ZrCp}_2\text{Cl}_x$ nanohybrid material. The information for the pore size and total pore volume in the nanomaterial is also accessible using the titled analysis. In this area, Fig. 10 shows the profile of N_2 adsorption-desorption for the composite system. Based on BDDT IUPAC classification, the shape of isotherm is closer to the isotherm of type IV with H3 hysteresis loop of desorption profile. This type of isotherm is a characteristic of mesoporous materials. In this context, the surface properties of $\text{rGO@Fe}_3\text{O}_4/\text{ZrCp}_2\text{Cl}_x$ system are summarized as $S_{\text{BET}} = 81.05 \text{ m}^2 \text{ g}^{-1}$, $V_{\text{m}} = 18.622 \text{ cm}^3 \text{ g}^{-1}$, average pore diameter = 11.358 nm and total pore volume = $0.2301 \text{ cm}^3 \text{ g}^{-1}$.

The magnetic property and value of Fe_3O_4 , $\text{rGO@Fe}_3\text{O}_4$ and $\text{rGO@Fe}_3\text{O}_4/\text{ZrCp}_2\text{Cl}_x$ composite systems were further studied using vibrating sample magnetometer (VSM) analysis in an external magnetic field up to 20 kOe at room temperature. The depicted graphs in Fig. 11 represent non-linear and reversible magnetic property for Fe_3O_4 (curve a), $\text{rGO@Fe}_3\text{O}_4$ (curve b) and $\text{rGO@Fe}_3\text{O}_4/\text{ZrCp}_2\text{Cl}_x$ (curve c). The saturation magnetization (M_{s}) values of Fe_3O_4 , $\text{rGO@Fe}_3\text{O}_4$ and $\text{rGO@Fe}_3\text{O}_4/\text{ZrCp}_2\text{Cl}_x$ are

respectively 75, 45 and 35 emu g^{-1} . The values clearly show that through combining Fe_3O_4 with rGO and then immobilization of ZrCp_2Cl_x , the magnetization value of $\text{rGO@Fe}_3\text{O}_4/\text{ZrCp}_2\text{Cl}_x$ was intensively diminished. Nevertheless, the magnetization value is still large enough for magnetic separation.

Catalytic activity of $\text{rGO@Fe}_3\text{O}_4/\text{ZrCp}_2\text{Cl}_x$ ($x = 0, 1, 2$) system

Reduction of nitroarenes to arylamines. Catalytic activity of $\text{rGO@Fe}_3\text{O}_4/\text{ZrCp}_2\text{Cl}_x$ nanocomposite system was studied by performing the reduction of nitroarenes with hydrazine hydrate 80% under different conditions. Primarily, the reaction conditions were optimized by examining the reduction of nitrobenzene as a model compound with $\text{N}_2\text{H}_4 \cdot \text{H}_2\text{O}$ 80% in the presence of $\text{rGO@Fe}_3\text{O}_4/\text{ZrCp}_2\text{Cl}_x$ using various solvents, varying the amounts of hydrazine hydrate and the nanocatalyst as well as the temperature of reaction. The results of this investigation are summarized in Table 1.

Investigation of the results exhibited that among the examined solvents including H_2O , EtOH, EtOH- H_2O (1 : 1), EtOAc and CH_3CN , the model reaction shows the perfect efficiency in refluxing EtOH using 20 mg of the nanocatalyst per 1 mmol of PhNO_2 (Table 1, entry 3). These examinations clearly represent that progress of the reduction reaction in protic solvents has higher rates and efficiency than aprotic ones. Although the exact mechanism for this influence is not clear, however, the better solvation of the nanocatalyst and nitro functionality as well as the presence of power hydrogen bonding ($\text{N} \cdots \text{H}$) between $\text{N}_2\text{H}_4 \cdot \text{H}_2\text{O}$ and the protic solvent (EtOH and H_2O) maybe play a role. All these cause the better transferring of hydrogen (from hydrazine) to nitro group to do the reduction reaction more easily. In the case of H_2O , low solubility of nitrobenzene in H_2O as a solvent proceeds the reaction with lower rate and efficiency.

Identifying the role of $\text{rGO@Fe}_3\text{O}_4/\text{ZrCp}_2\text{Cl}_x$ nanocomposite system for catalyzing the reduction reaction was also carried out by examining the model reaction in the presence of $\text{rGO@Fe}_3\text{O}_4$ and ZrCp_2Cl_2 (Table 1). Entries 10–12 clearly show that using $\text{rGO@Fe}_3\text{O}_4$ and ZrCp_2Cl_2 catalyst systems did not progress the reaction efficiently. It is therefore concluded that the

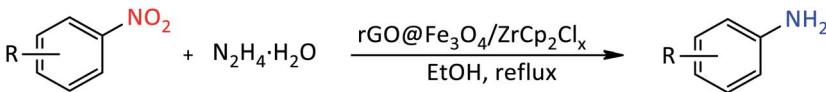
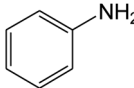
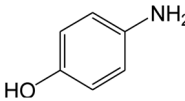
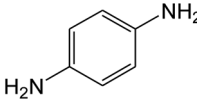
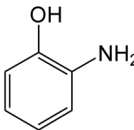
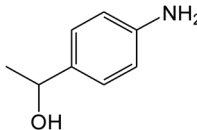
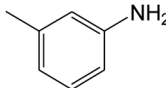
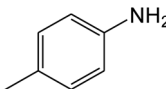
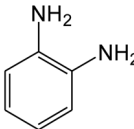
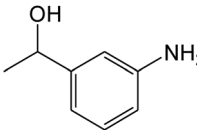
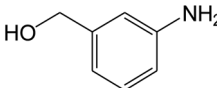
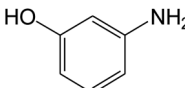
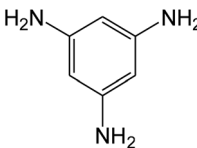
Table 1 Optimization experiments for reduction of nitrobenzene to aniline with $\text{N}_2\text{H}_4 \cdot \text{H}_2\text{O}/\text{rGO@Fe}_3\text{O}_4/\text{ZrCp}_2\text{Cl}_x$ ($x = 0, 1, 2$) system^a

Entry	Catalyst	Amount (mg)	$\text{N}_2\text{H}_4 \cdot \text{H}_2\text{O}$ (mmol)	Condition	Time (min)	Yield (%)
1	$\text{rGO@Fe}_3\text{O}_4/\text{ZrCp}_2\text{Cl}_x$ ($x = 0, 1, 2$)	20	2	EtOH, r.t.	60	55
2	$\text{rGO@Fe}_3\text{O}_4/\text{ZrCp}_2\text{Cl}_x$ ($x = 0, 1, 2$)	10	2	EtOH, reflux	60	60
3	$\text{rGO@Fe}_3\text{O}_4/\text{ZrCp}_2\text{Cl}_x$ ($x = 0, 1, 2$)	20	2	EtOH, reflux	10	100
4	$\text{rGO@Fe}_3\text{O}_4/\text{ZrCp}_2\text{Cl}_x$ ($x = 0, 1, 2$)	30	2	EtOH, reflux	10	70
5	$\text{rGO@Fe}_3\text{O}_4/\text{ZrCp}_2\text{Cl}_x$ ($x = 0, 1, 2$)	20	1	EtOH, reflux	10	60
6	$\text{rGO@Fe}_3\text{O}_4/\text{ZrCp}_2\text{Cl}_x$ ($x = 0, 1, 2$)	20	2	H_2O , 70 °C	60	60
7	$\text{rGO@Fe}_3\text{O}_4/\text{ZrCp}_2\text{Cl}_x$ ($x = 0, 1, 2$)	20	2	H_2O -EtOH (1 : 1), 70 °C	60	50
8	$\text{rGO@Fe}_3\text{O}_4/\text{ZrCp}_2\text{Cl}_x$ ($x = 0, 1, 2$)	20	2	EtOAc, reflux	60	20
9	$\text{rGO@Fe}_3\text{O}_4/\text{ZrCp}_2\text{Cl}_x$ ($x = 0, 1, 2$)	20	2	CH_3CN , reflux	60	30
10	$\text{rGO@Fe}_3\text{O}_4$	20	2	EtOH, reflux	60	8
11	ZrCp_2Cl_2	20	2	EtOH, reflux	60	20
12	ZrCp_2Cl_2	20	2	H_2O , reflux	60	10
13	—	—	2	EtOH, reflux	120	Trace

^a All reactions were carried out with 1 mmol of nitrobenzene in 2 mL solvent.



Table 2 Catalytic activity of the nanocatalyst for the reduction of nitrobenzene to aniline with $N_2H_4 \cdot H_2O$ 80%^a

				
Entry	R	Product	Time (min)	Yield (%)
1	H		10	98
2	4-OH		30	90
3	4-NH ₂		40	98
4	2-OH		15	97
5	4-COMe		20	92
6	3-Me		35	90
7	4-Me		30	91
8	2-NH ₂		60	95
9	3-COMe		45	94
10	3-CHO		60	93
11	3-OH		30	96
12 ^b	3-NH ₂ -5-NO ₂		20	92

^a All reactions were carried out with 1 mmol of nitroarene, 2 mmol of $N_2H_4 \cdot H_2O$ 80% and 20 mg of $rGO@Fe_3O_4/ZrCp_2Cl_x$ in refluxing EtOH (2 mL).^b In this reaction 3 mmol of $N_2H_4 \cdot H_2O$ 80% was used.

Table 3 Reductive-acetylation of nitroarenes to *N*-arylacetamides using $\text{N}_2\text{H}_4 \cdot \text{H}_2\text{O}/\text{rGO@Fe}_3\text{O}_4/\text{ZrCp}_2\text{Cl}_x/\text{Ac}_2\text{O}$ system^a

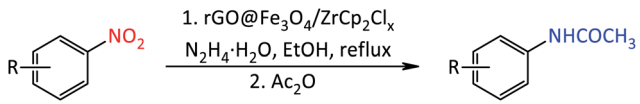
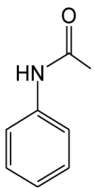
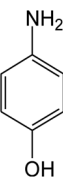
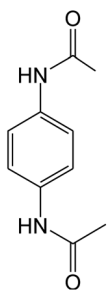
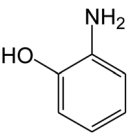
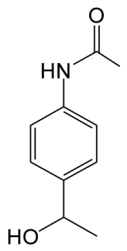
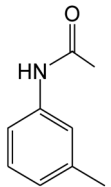
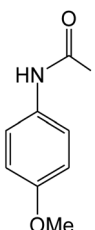
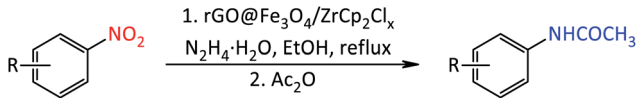
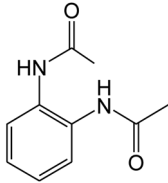
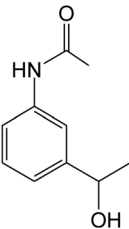
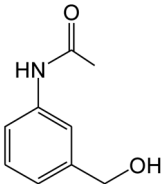
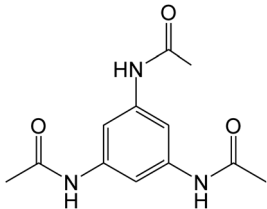
				
Entry	R	Product	Time (min)	Yield (%)
1	H		15	97
2	4-OH		100	No reaction
3	4-NH ₂		50	98
4	2-OH		25	No reaction
5	4-COMe		30	50
6	3-Me		40	95
7	4-OMe		40	94



Table 3 (Contd.)



Entry	R	Product	Time (min)	Yield (%)
8	2-NH ₂		70	97
9	3-COMe		55	60
10	3-CHO		70	70
12 ^b	3-NH ₂ -5-NO ₂		30	91

^a All reactions were carried out with 1 mmol of nitroarene, 2 mmol of N₂H₄·H₂O 80%, 2 mmol Ac₂O and 20 mg of rGO@Fe₃O₄/ZrCp₂Cl_x in refluxing EtOH (2 mL). ^b In this reaction, 3 mmol of N₂H₄·H₂O 80% and Ac₂O was used.

multicatalysts activity of Fe₃O₄, zirconium species as well as rGO and the extreme surface area and mesopore structural characteristic of rGO@Fe₃O₄/ZrCp₂Cl_x synergistically accomplish the reduction reaction in shorter reaction time.

The examination for doing reduction of PhNO₂ with sodium borohydride or isopropanol as the other commercially available reductants in the presence of rGO@Fe₃O₄/ZrCp₂Cl_x composite system did not show the reasonable results. The study was therefore continued by performing the reduction reactions with hydrazine hydrate 80% at the optimized conditions (Table 1, entry 3).

The scope and capability of rGO@Fe₃O₄/ZrCp₂Cl_x composite system to catalyze reduction of nitro functionality was further studied by performing the reduction of diverse aromatic nitro compounds with N₂H₄·H₂O 80% at the optimized reaction conditions. The results of this investigation are summarized in

Table 2. The table represents that various nitroarenes containing electron-releasing and withdrawing groups as well as aldehyde and ketone functionalities were reduced using 2 mmol of N₂H₄·H₂O 80% in refluxing EtOH. All reactions were carried out with 15–60 min to afford the aniline products in high yields. In the case of nitro compounds containing carbonyl functionality (entries 5, 9 and 10), the reduction reactions were carried out without any selectivity and both of nitro and carbonyl groups were reduced using 2 mmol of N₂H₄·H₂O 80% in the presence of rGO@Fe₃O₄/ZrCp₂Cl_x (20 mg) giving the corresponding aniline products with the alcohol functionality.

Reductive-acetylation of nitroarenes. Direct synthesis of amides from the one-pot reductive-acetylation of nitro compounds is one of the significant reactions in organic synthesis. In this context and due to importance of the amide functionality in widely synthesis of agricultural and

Table 4 *N*-Acetylation of arylamines using rGO@Fe₃O₄/ZrCp₂Cl_x/Ac₂O system^a

$\text{R}-\text{C}_6\text{H}_4-\text{NH}_2 + \text{Ac}_2\text{O} \xrightarrow[\text{EtOH, reflux}]{\text{rGO@Fe}_3\text{O}_4/\text{ZrCp}_2\text{Cl}_x} \text{R}-\text{C}_6\text{H}_4-\text{NHCOCH}_3$				
Entry	R	Product	Time (min)	Yield (%)
1	H		5	97
2	4-MeO		10	98
3	4-Cl		5	96
4	4-Me		10	97
5	3-NH ₂		10	94
6	2-Me-3-Cl		5	93



Table 4 (Contd.)

$\text{R}-\text{C}_6\text{H}_4\text{NH}_2 + \text{Ac}_2\text{O} \xrightarrow[\text{EtOH, reflux}]{\text{rGO@Fe}_3\text{O}_4/\text{ZrCp}_2\text{Cl}_x} \text{R}-\text{C}_6\text{H}_4\text{NHCOCH}_3$				
Entry	R	Product	Time (min)	Yield (%)
7	2-NH ₂ -4-Me		15	91
8	2-NO ₂		10	96
9	4-OH		60	No reaction
10	3-COMe		10	88

^a All reactions were carried out with 1 mmol of arylamine, 2 mmol Ac₂O and 20 mg of rGO@Fe₃O₄/ZrCp₂Cl_x in refluxing EtOH (2 mL).

pharmaceutical materials, we therefore prompted to investigate the capability of N₂H₄·H₂O/rGO@Fe₃O₄/ZrCp₂Cl_x/Ac₂O system towards the titled transformation. In this context, when the reduction of nitrobenzene at the optimized reaction conditions (Table 1, entry 3) was completed, Ac₂O (2 mmol) was added to the reaction mixture without isolation of the produced aniline. After that, progress of the reaction mixture was continued under reflux conditions for 5 min to afford acetanilide in 97% yield (Table 3, entry 1). It is notable that the total time for the mentioned transformation take place for 15 min (10 min for the reduction reaction + 5 min for the acetylation reaction).

Based on the obtained accessibility, therefore, the generality of this synthetic method was further investigated by performing reductive-acetylation of the all examined nitroarenes (at the previous section) to the corresponding *N*-arylacetamides

through adding 2 mmol acetic anhydride to the reaction mixture. The results of this investigation are summarized in Table 3. The table shows that most of the examined nitro functionalities were successfully converted to the corresponding amides in high yields at the optimized reaction conditions. In addition, the compounds containing phenolic functionality in the presence of amino group did not take place acetylation of the amino or phenolic groups, and therefore the produced aminophenol material was recovered from the reaction mixture. Although the exact explanation for this inability is not known, however, this maybe due to the formation of zwitter ion through the acidic and basic characteristic of phenol and amine groups which prevent the progress of the acetylation reaction towards formation of the amide product. Moreover, in the case of the materials containing amino and alcoholic groups, only



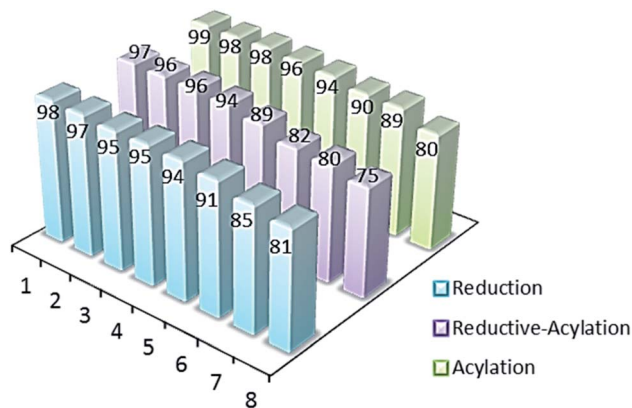


Fig. 12 Recycling of $\text{rGO@Fe}_3\text{O}_4/\text{ZrCp}_2\text{Cl}_x$ ($x = 0, 1, 2$) nanohybrid material in reduction and reductive-acetylation of nitrobenzene and *N*-acetylation of aniline.

acetylation of the amine functionality was carried out and accordingly the hydroxy group was remained intact. It is therefore concluded that $\text{N}_2\text{H}_4 \cdot \text{H}_2\text{O}/\text{rGO@Fe}_3\text{O}_4/\text{ZrCp}_2\text{Cl}_x/\text{Ac}_2\text{O}$ system has a selectivity among alcoholic and amino groups towards the acetylation reaction.

Acylation of arylamines. The successful reductive-acetylation of structurally diverse aromatic nitro compounds by $\text{N}_2\text{H}_4 \cdot \text{H}_2\text{O}/\text{rGO@Fe}_3\text{O}_4/\text{ZrCp}_2\text{Cl}_x/\text{Ac}_2\text{O}$ system encouraged us to study the capability of $\text{rGO@Fe}_3\text{O}_4/\text{ZrCp}_2\text{Cl}_x$ composite system towards acetylation of commercially available arylamines using acetic anhydride at the next step. Based on the obtained results for the optimization experiments at the previous sections, the acetylation of aniline (1 mmol) with Ac_2O (2 mmol) in the presence of 20 mg $\text{rGO@Fe}_3\text{O}_4/\text{ZrCp}_2\text{Cl}_x$ composite system was carried out successfully in refluxing EtOH. The reaction was completed within 5 min to afford acetanilide in 97% yield (Table 4, entry 1). Accordingly, arylamines containing electron-releasing and withdrawing substituents were successfully reacted with acetic anhydride (2 mmol) in the presence of $\text{rGO@Fe}_3\text{O}_4/\text{ZrCp}_2\text{Cl}_x$ composite system (20 mg) to afford the corresponding *N*-arylamides within 5–15 min in high yields (Table 4). The case study in Table 4 shows that electron-releasing substituents progress the acetylation reaction in higher rates (shorter reaction times) than the electron-withdrawing ones. As well, 4-aminophenol under the examined reaction conditions, did not take place the acetylation reaction (entry 9). As the above mentioned, the reason with more probability is due to the formation of zwitter ion derived by acidic and basic character of phenol and amino groups. This explanation was evidenced by

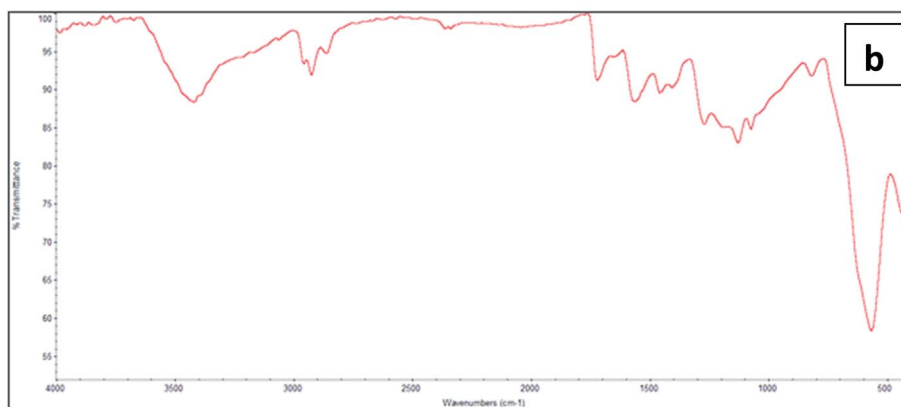
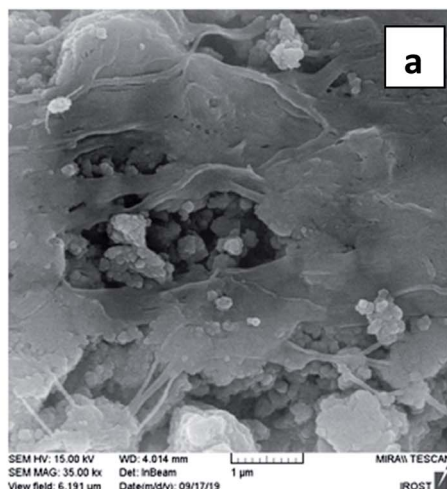


Fig. 13 SEM image (a) and FT-IR spectrum (b) of the recycled $\text{rGO@Fe}_3\text{O}_4/\text{ZrCp}_2\text{Cl}_x$ ($x = 0, 1, 2$).



Table 5 Comparison of the catalytic activity of $\text{rGO}@Fe_3O_4/\text{ZrCp}_2\text{Cl}_x$ for reduction of nitroarenes with other reported catalyst systems

Entry	Catalyst (mg)	Reductant	Time	Yield (%)	Conditions	Ref.
1	Present work	$\text{N}_2\text{H}_4 \cdot \text{H}_2\text{O}$	10 min	95–100	20 mg, EtOH, 70 °C	—
2	Fe-phen/C-800	H_2 (g)	15 h	90–96	50 bar H_2 , H_2O -THF, 120 °C	79
3	$\text{Co}_3\text{O}_4@Al_2\text{O}_3/\text{SiO}_2$	$\text{N}_2\text{H}_4 \cdot \text{H}_2\text{O}$	2 h	90–100	2 mol%, EtOH, 60 °C	80
4	Ru-CNT	$\text{N}_2\text{H}_4 \cdot \text{H}_2\text{O}$	3 h	95–100	N_2 atm, THF, r.t.	81
5	Iron oxide hydroxide $[\text{FeO}(\text{OH})]$	$\text{N}_2\text{H}_4 \cdot \text{H}_2\text{O}$	5 h	95–100	30 mg, EtOH, 70 °C	82
6	$\text{rGO}/\text{Cu}_2\text{O}-\text{CuO}$	$\text{N}_2\text{H}_4 \cdot \text{H}_2\text{O}$	2–3 h	95–100	50 mg, $\text{MeOH}-\text{CH}_2\text{Cl}_2-\text{CH}_3\text{CN}$ visible light, r.t.	83
7	rGO/BiVO_4	$\text{N}_2\text{H}_4 \cdot \text{H}_2\text{O}$	1–2 h	95–100	50 mg, visible light, r.t.	84
8	$\text{Ir}/\text{ZrO}_2 \cdot x\text{H}_2\text{O}$	H_2 (g)	2–3 h	95–100	25 mg, EtOH- H_2O , 1 atm	85
9	$\text{Au}@Zr\text{-phosphonate}$	NaBH_4	2–3 h	80–90	2 mol%, EtOH, 30 °C	86

the successful acetylation of 4-methoxyaniline with Ac_2O catalyzed by the nanocomposite of $\text{rGO}@Fe_3O_4/\text{ZrCp}_2\text{Cl}_x$ to afford 4-methoxyacetanilide in 98% yield within 10 min. In this material 4-methoxy substituent is the protected form of 4-hydroxy functionality. Therefore, the acidic character of phenolic functionality was omitted through the replacement with 4-methoxy group. As a result, 4-methoxyaniline has no any capability to form zwitter ion characteristic and so in contrast to 4-amino-phenol material perform the acetylation reaction perfectly.

Recycling of $\text{rGO}@Fe_3O_4/\text{ZrCp}_2\text{Cl}_x$ ($x = 0, 1, 2$) nanohybrid material

Recovery and reusability of the heterogeneous catalyst systems is one of the crucial subjects from the prospects of economic and environment. Evaluation of this capability for $\text{rGO}@Fe_3O_4/\text{ZrCp}_2\text{Cl}_x$ nanocomposite system was carried out by recovering of the nanocatalyst and then reusing it for the further examinations. In this context, when reduction and reductive-acetylation of nitrobenzene as well as acetylation of aniline in the presence of $\text{rGO}@Fe_3O_4/\text{ZrCp}_2\text{Cl}_x$ composite system was completed, the nanocatalyst was magnetically recovered from the reaction mixture and then washed with EtOH. After drying under air atmosphere, the recovered nanocatalyst was reused for the next runs of the mentioned transformations. The depicted graphs in Fig. 12 show that after 8 consecutive recycling, $\text{rGO}@Fe_3O_4/\text{ZrCp}_2\text{Cl}_x$ composite system has the acceptable activity to promote the transformation reactions. In this context, FT-IR spectrum and SEM analysis of the recovered nanocatalyst system after 8 reusing cycles represent a slightly change of the morphology and mesoporosity of the surface (Fig. 13).

Hot filtration

From the aspects of sustainability and green chemistry, stability and recyclability of the catalyst systems are the desirable characteristics. To illustrate the heterogeneous and structural stability of $\text{rGO}@Fe_3O_4/\text{ZrCp}_2\text{Cl}_x$ nanohybrid material, a hot filtration examination was carried out through performing the reduction of PhNO_2 with hydrazine hydrate within 10 min at the optimized reaction conditions (1 mmol PhNO_2 , 2 mmol $\text{N}_2\text{H}_4 \cdot \text{H}_2\text{O}$ 80% and 20 mg of the nanocatalyst in refluxing EtOH). Monitoring of the model reaction showed that in the meantime of 5 min (half of the reaction time), the reduction reaction was progressed for 70%. Next, the magnetic

nanohybrid catalyst system was removed from the reaction mixture (using an external magnetic field) and then the reaction was allowed to continue in refluxing EtOH with reducing agent. Progress of the reaction was monitored after 120 min to evaluate the reduction of nitrobenzene in the absence of the nanocatalyst system. It was found that only a trace reduction of PhNO_2 (<2%) was carried out upon refluxing ethanolic solution and catalyst-free condition of the reaction mixture. This examination clearly reveals that $\text{rGO}@Fe_3O_4/\text{ZrCp}_2\text{Cl}_x$ nanohybrid material has the negligible leaching which proves its high stability. In this context, after removing $\text{rGO}@Fe_3O_4/\text{ZrCp}_2\text{Cl}_x$ composite system in a meanwhile of the hot-filtration examination, ICP-OES analysis for the remaining Zr species in the reaction mixture showed 3% leaching of the nanocatalyst material.

In addition, catalytic activity of $\text{rGO}@Fe_3O_4/\text{ZrCp}_2\text{Cl}_x$ nanocatalyst system for the reduction of nitroarenes with hydrazine hydrate 80% was highlighted by comparison of the obtained results with those of previously reported other catalysts systems (Table 5). A case study shows that in terms of reaction time and conditions, yield of the products, the current protocol represents a more or comparable efficiency than the previous systems.

Conclusion

In this paper, the immobilization of zirconocene on magnetite-reduced graphene oxide was investigated to afford the novel $\text{rGO}@Fe_3O_4/\text{ZrCp}_2\text{Cl}_x$ ($x = 0, 1, 2$) nanohybrid material. The prepared composite system was then characterized using FT-IR, SEM, EDX, VSM, ICP-OES, TGA, BET and MS analyses. Next, catalytic activity of the nanocomposite was studied towards reduction and reductive-acetylation of nitroarenes as well as *N*-acetylation of arylamines. Reduction and reductive acetylation of nitroarenes was carried out by $\text{N}_2\text{H}_4 \cdot \text{H}_2\text{O}$ 80% and $\text{N}_2\text{H}_4 \cdot \text{H}_2\text{O}$ 80%/Ac₂O, respectively. As well, *N*-acetylation of arylamines was taken place with acetic anhydride in the presence of the nanocatalyst system. All reactions were accomplished in refluxing EtOH as a green solvent giving arylamines and *N*-arylacetamides in high yields. Recovery and reusability of $\text{rGO}@Fe_3O_4/\text{ZrCp}_2\text{Cl}_x$ ($x = 0, 1, 2$) was also carried out for 8 consecutive cycles without the significant loss of the catalytic activity.



Experimental section

Chemicals and instruments

All reagents and materials were purchased from chemical sources and they were used without further purification. A Bruker Vertex 70 spectrometer was used to record Fourier transform infrared spectra of the materials. ^1H and ^{13}C NMR spectra were recorded on 250/400 MHz Bruker spectrometer. X-ray diffraction (XRD) measurements were fulfilled on X'Pert Pro Panalytical diffractometer in 40 kV/30 mA with a Cu K α radiation ($\lambda = 1.5418 \text{ \AA}$). Signal data were recorded in $2\theta = 10\text{--}80^\circ$ with a step interval of 0.05° . A FESEM-TESCAN MIRA3 apparatus was utilized to determine the morphology and size distribution of particles by scanning electron microscopy (SEM) method. This apparatus was also used to reveal the chemical composition and elemental mapping of the nanocatalyst through energy-dispersive X-ray spectroscopy (EDX) technique. The BET (Brunauer–Emmett–Teller) surface area, pore volume and pore diameter of the samples were measured using Nova Station B, Quantachrome Instrument, USA. The thermogravimetric analysis (TGA) pattern was recorded using Shimadzu DTG-60 instrument. Vibrating sample magnetometer (VSM, Meghnatis Daghigh Kavir Co., Iran) analysis under magnetic field up to 20 kOe was applied to determine the magnetic property of the samples. Mass spectrometry measurement was recorded using Agilent Technology (HP) Model: 5973 network mass selective detector. Elemental analysis of Zr was carried out by inductively coupled plasma-optical emission spectrometry (ICP-OES) model ARCOS, Germany. Thin layer chromatography (TLC) was utilized to determine the purity of the products and to monitor the progress of the reactions using SILG/UV 254 aluminum sheets.

Synthesis of reduced graphite oxide (rGO) nanosheets

rGO was synthesized from graphite by the already reported procedure.⁸⁷ In a typical procedure, 1 g of graphite flakes was added to 50 mL concentrated sulfuric acid 98%, while stirring in an ice-water bath. 3 g potassium permanganate was gradually added by maintaining the temperature under 10°C . Then, the suspension was stirred at room temperature for 25 min followed by 5 min sonication in an ultrasonic bath. After repeating the stirring-sonication process for 12 times, the reaction was quenched by the addition of 200 mL distilled water and 2 h more sonication. After adjusting the pH at 6, the suspension was further sonicated for 1 h. 10 g L-ascorbic acid was dissolved in 100 mL distilled water and then was slowly added to the exfoliated graphite oxide suspension at room temperature. The reduction was performed at 95°C for 1 h. The resultant black precipitates were simply filtered by cellulose filter paper and were further washed with hydrochloric acid (1 M) and distilled water to gain neutral pH. The filtrate was finally freeze-dried to obtain rGO powder.

Preparation of rGO@Fe₃O₄ nanohybrid

0.8 g of the obtained rGO was dispersed in 50 mL distilled water by sonication for 2 min. Then, an aqueous solution of FeCl₃·6H₂O (1.9 g) and FeCl₂·4H₂O (1.4 g) in 30 mL of distilled water

was added to the dispersion of rGO followed by sonication for 5 min. Next, a solution of 40 mL ammonia 25% and 20 mL distilled water was added to the prepared mixture in dropwise manner and continuous stirring under N₂ atmosphere for 1 h. The resulting mixture was stirred for 30 min and then filtered, washed with distilled water and dried in oven at 60°C for 2 h.

Preparation of rGO@Fe₃O₄/ZrCp₂Cl_x ($x = 0, 1, 2$) nanocomposite

0.5 g of magnetically nanoparticles of rGO@Fe₃O₄ was dispersed in 50 mL of benzene by sonication for 1 min. Then, a solution of the dissolved ZrCp₂Cl₂ (0.1 g) in 50 mL of benzene was added to the solution of rGO@Fe₃O₄ and the resulting mixture was stirred for 24 h at 50°C . The prepared rGO@Fe₃O₄/ZrCp₂Cl_x nanocomposite system were magnetically separated and washed with ethanol and deionized water followed by drying at room temperature under vacuum.

A general procedure for reduction of nitroarenes with N₂H₄·H₂O and rGO@Fe₃O₄/ZrCp₂Cl_x ($x = 0, 1, 2$) system

In a round-bottom flask equipped with a magnetic stirrer, a mixture of nitroarene (1 mmol), rGO@Fe₃O₄/ZrCp₂Cl_x (20 mg) and ethanol (2 mL) was prepared. Then, N₂H₄·H₂O (80%, solution in water, 2 mmol) was added and the resulting mixture was stirred under reflux conditions. Progress of the reaction was monitored by TLC. After completion of the reaction, the magnetic nanocatalyst was separated using an external magnetic field and the mixture was then extracted with EtOAc. The combined organic layers were dried over anhydrous Na₂SO₄. Evaporation of the solvent under reduced pressure affords the corresponding arylamine product.

A general procedure for reductive-acetylation of nitroarenes with N₂H₄·H₂O/rGO@Fe₃O₄/ZrCp₂Cl_x/Ac₂O system

In a round-bottom flask equipped with a magnetic stirrer, a mixture of nitroarene (1 mmol), N₂H₄·H₂O (80%) (2 mmol) and rGO@Fe₃O₄/ZrCp₂Cl_x (20 mg) in ethanol (2 mL) was prepared. Progress of the reduction reaction was carried out for an appropriate time (mentioned in Table 2) under reflux conditions. After that, Ac₂O (2 mmol) was added and the resulting mixture was stirred to accomplish *N*-acetylation of the *in situ* prepared arylamines in refluxing EtOH. Magnetically nanoparticles of rGO@Fe₃O₄/ZrCp₂Cl_x were separated using an external magnetic field and the mixture was then extracted with EtOAc. The combined organic layers were dried over anhydrous Na₂SO₄. Evaporation of the solvent under reduced pressure gave the corresponding *N*-arylacetamides.

A general procedure for acetylation of arylamines with rGO@Fe₃O₄/ZrCp₂Cl_x/Ac₂O system

In a round-bottom flask equipped with a magnetic stirrer, a mixture of arylamine (1 mmol), Ac₂O (2 mmol) and rGO@Fe₃O₄/ZrCp₂Cl_x (20 mg) in ethanol (2 mL) was prepared. The resulting mixture was stirred under reflux conditions for an appropriate time mentioned in Table 4. After completion of the reaction (monitored by TLC), magnetically nanoparticles of



rGO@Fe₃O₄/ZrCp₂Cl_x were separated using an external magnetic field and the mixture was then extracted with EtOAc. The combined organic layers were dried over anhydrous Na₂SO₄. Evaporation of the solvent under reduced pressure gave the corresponding *N*-arylacetamides.

Funding

Research Council of Urmia University.

Author contributions

Massood Bayzidi: formal analysis; investigation; methodology; project administration.

Behzad Zeynizadeh: conceptualization; funding acquisition; project administration; supervision.

Conflicts of interest

The authors declare no conflicts of interest.

Acknowledgements

The authors gratefully appreciated the financial support of this work by the Research Council of Urmia University.

References

- 1 M. D. Jones, *Sustainable Catalysis with Non-endangered Metals*, ed. M. North, Royal Society of Chemistry, Yurk, 2016, vol. 2, pp. 199–212.
- 2 (a) L. Resconi, F. Piemontesi, G. Franciscano, L. Abis and T. Fiorani, *J. Am. Chem. Soc.*, 1992, **114**, 1025–1032; (b) G. J. P. Britovsek, V. C. Gibson and D. F. Wass, *Angew. Chem., Int. Ed. Engl.*, 1999, **38**, 428–447.
- 3 (a) K. de la Vega-Hernández, R. Senatore, M. Miele, E. Urban, W. Holzer and V. Pace, *Org. Biomol. Chem.*, 2019, **17**, 1970–1978; (b) J. T. Spletstoser, J. M. White, A. R. Tunoori and G. I. Georg, *J. Am. Chem. Soc.*, 2007, **129**, 3408–3419; (c) V. Pace, K. de la Vega-Hernández, E. Urban and T. Langer, *Org. Lett.*, 2016, **18**, 2750–2753; (d) C. Matt, F. Kölblin and J. Streuff, *Org. Lett.*, 2019, **21**, 6983–6988.
- 4 J. A. Miller and E. Negishi, *Tetrahedron Lett.*, 1984, **25**, 5863–5866.
- 5 H. Makabe and E. Negishi, *Eur. J. Org. Chem.*, 1999, **1999**, 969–971.
- 6 B. H. Lipshutz and E. L. Ellsworth, *J. Am. Chem. Soc.*, 1990, **112**, 7440–7441.
- 7 Z. Huang and E. Negishi, *Org. Lett.*, 2006, **8**, 3675–3678.
- 8 H. Tsuneaki and M. Osamu, *Chem. Lett.*, 1975, **4**, 259–260.
- 9 P. Barbaro and F. Liguori, *Heterogenized Homogeneous Catalysts for Fine Chemicals Production: Catalysis by Metal Complexes*, Springer, Dordrecht, 2010, vol. 33.
- 10 T. Tamoradi, S. M. Mousavi and M. Mohammadi, *New J. Chem.*, 2020, **44**, 8289–8302.
- 11 (a) M. Kazemi and M. Mohammadi, *Appl. Organomet. Chem.*, 2020, **34**, e5400; (b) L. M. Rossi, N. J. S. Costa, F. P. Silva and R. Wojcieszak, *Green Chem.*, 2014, **16**, 2906–2933.
- 12 M. Nasr-Esfahani, S. J. Hoseini, M. Montazerzohori, R. Mehrabi and H. Nasrabadi, *J. Mol. Catal. A: Chem.*, 2014, **382**, 99–105.
- 13 C. Yang, J. Wu and Y. Hou, *Chem. Commun.*, 2011, **47**, 5130–5141.
- 14 S. Iraqui, S. S. Kashyap and M. H. Rashid, *Nanoscale Adv.*, 2020, **2**, 5790–5802.
- 15 S. Sharifi, A. Yazdani and K. Rahimi, *Sci. Rep.*, 2020, **10**, 10916.
- 16 C. Simon, M. B. Zakaria, H. Kurz, D. Tetzlaff, A. Blösser, M. Weiss, J. Timm, B. Weber, U.-P. Apfel and R. Marschall, *Chem.–Eur. J.*, 2021, **27**, 16990–17001.
- 17 M. Houshiar, F. Zebhi, Z. J. Razi, A. Alidoust and Z. Askari, *J. Magn. Magn. Mater.*, 2014, **371**, 43–48.
- 18 R. Eisavi, S. Ghadernejad, B. Zeynizadeh and F. Mohammad Aminzadeh, *J. Sulfur Chem.*, 2016, **37**, 537–545.
- 19 K. Baruah, A. Kant, P. Gaijon, S. Ghosh and M. R. Singh, *Appl. Surf. Sci. Adv.*, 2021, **6**, 100130.
- 20 R. Eivazzadeh-Keihan, S. Asgharnasl, M. S. Bani, F. Radinekiyan, A. Maleki, M. Mahdavi, P. Babaniamansour, H. Bahreinizad, A. E. Shalan and S. Lancers-Méndez, *Langmuir*, 2021, **37**, 8847–8854.
- 21 N. Akhlaghi and G. Najafpour-Darzi, *J. Ind. Eng. Chem.*, 2021, **103**, 292–304.
- 22 S. Taghavi Fardood, A. Ramazani, Z. Golfar and S. W. Joo, *Appl. Organomet. Chem.*, 2017, **31**, e3823.
- 23 N. Wang, X. Luo, L. Han, Z. Zhang, R. Zhang, H. Olin and Y. Yang, *Nano-Micro Lett.*, 2020, **12**, 81.
- 24 A. Ghorbani-Choghamarani, M. Mohammadi, L. Shiri and Z. Taherinia, *Res. Chem. Intermed.*, 2019, **45**, 5705–5723.
- 25 M. Taei, F. Hasanpour, M. Movahedi and S. Mohammadian, *RSC Adv.*, 2015, **5**, 37431–37439.
- 26 X. W. Lou and L. A. Archer, *Adv. Mater.*, 2008, **20**, 1853–1858.
- 27 (a) A. Ghorbani-Choghamarani, M. Mohammadi and Z. Taherinia, *J. Iran. Chem. Soc.*, 2019, **16**, 411–421; (b) W. Chiu, P. Khiew, M. Cloke, D. Isa, H. Lim, T. Tan, N. Huang, S. Radiman, R. Abd-Shukor and M. A. A. Hamid, *J. Phys. Chem. C*, 2010, **114**, 8212–8218.
- 28 H. Peng, X. Wang, C. J. Hu and X. Tian, *New J. Chem.*, 2016, **40**, 7911–7916.
- 29 A. Khazaei, M. Khazaei and M. Nasrollahzadeh, *Tetrahedron*, 2017, **73**, 5624–5633.
- 30 Z. Arabpoor and H. R. Shaterian, *RSC Adv.*, 2016, **6**, 44459–44468.
- 31 (a) M. Gilanizadeh and B. Zeynizadeh, *Polycyclic Aromat. Compd.*, 2021, **41**, 15–32; (b) L. Ding, L. Yang, J. Xu, J. Zheng and M. Zhang, *Inorg. Chem.*, 2021, **60**, 8880–8889.
- 32 B. Zeynizadeh, M. Sadeghbari and N. N. Pesyan, *Curr. Org. Synth.*, 2019, **16**, 1010–1023.
- 33 S. Xuan, Y.-X. J. Wang, J. C. Yu and K. C.-F. Leung, *Langmuir*, 2009, **25**, 11835–11843.
- 34 D. Rosario-Amorin, M. Gaboyard, R. Clérac, L. Vellutini, S. Nlate and K. Heuzé, *Chem.–Eur. J.*, 2012, **18**, 3305–3315.



- 35 A. Schätz, T. R. Long, R. N. Grass, W. J. Stark, P. R. Hanson and O. Reiser, *Adv. Funct. Mater.*, 2010, **20**, 4323–4328.
- 36 M. Esmati and B. Zeynizadeh, *Appl. Organomet. Chem.*, 2022, **36**, e6496.
- 37 M. Alvand and F. Shemirani, *Microchim. Acta*, 2016, **183**, 1749–1757.
- 38 J. Guo, H. Jiang, Y. Teng, Y. Xiong, Z. Chen, L. You and D. Xiao, *J. Mater. Chem. B*, 2021, **9**, 9076–9099.
- 39 M. Zhang, L. Ding, J. Zheng, L. Liu, H. Alsulami, M. A. Kutbi and J. Xu, *Appl. Surf. Sci.*, 2020, **509**, 145348.
- 40 C. R. Minitha, R. Suresh, U. K. Maity, Y. Haldorai, V. Subramaniam, P. Manoravi, M. Joseph and R. T. Rajendra Kumar, *Ind. Eng. Chem. Res.*, 2018, **57**, 1225–1232.
- 41 P. Ghamari Kargar, G. Bagherzade and H. Eshghi, *RSC Adv.*, 2020, **10**, 32927–32937.
- 42 S. Mallakpour and M. Madani, *Prog. Org. Coat.*, 2015, **86**, 194–207.
- 43 S. Rouhani, A. Rostami and A. Salimi, *RSC Adv.*, 2016, **6**, 26709–26718.
- 44 M. Yarie, M. A. Zolfigol, Y. Bayat, A. Asgari, D. A. Alonso and A. Khoshnood, *RSC Adv.*, 2016, **6**, 82842–82853.
- 45 R. Taheri-Ledari, J. Rahimi and A. Maleki, *Ultrason. Sonochem.*, 2019, **59**, 104737.
- 46 L. Shiri, S. Zarei, M. Kazemi and D. Sheikh, *Appl. Organomet. Chem.*, 2018, **32**, e3938.
- 47 B. Zeynizadeh, S. Rahmani and E. Eghbali, *Polyhedron*, 2019, **168**, 57–66.
- 48 (a) Y. Zhang, S. Liu, W. Lu, L. Wang, J. Tian and X. Sun, *Catal. Sci. Technol.*, 2011, **1**, 1142–1144; (b) D. Shan, S. Deng, C. Jiang, Y. Chen, B. Wang, Y. Wang, J. Huang, G. Yu and M. R. Wiesner, *Environ. Sci.: Nano*, 2018, **5**, 1650–1660; (c) S. Mahalingam and Y.-H. Ahn, *New J. Chem.*, 2018, **42**, 4372–4383; (d) C. Ding, W. Wei, H. Sun, J. Ding, J. Ren and X. Qu, *Carbon*, 2014, **79**, 615–622.
- 49 D. C. Marcano, D. V. Kosynkin, J. M. Berlin, A. Sinitskii, Z. Sun, A. Slesarev, L. B. Alemany, W. Lu and J. M. Tour, *ACS Nano*, 2010, **4**, 4806–4814.
- 50 J. Pyun, *Angew. Chem., Int. Ed.*, 2011, **50**, 46–48.
- 51 D. R. Dreyer, H.-P. Jia and C. W. Bielawski, *Angew. Chem., Int. Ed.*, 2010, **49**, 6813–6816.
- 52 B. Majumdar, D. Sarma, T. Bhattacharya and T. K. Sarma, *ACS Sustainable Chem. Eng.*, 2017, **5**, 9286–9294.
- 53 D. Sengupta, S. Ghosh and B. Basu, *Curr. Org. Chem.*, 2017, **21**, 834–854.
- 54 D. Higgins, P. Zamani, A. Yu and Z. Chen, *Energy Environ. Sci.*, 2016, **9**, 357–390.
- 55 C. Feng, H. Y. Zhang, N. Z. Shang, S. T. Gao and C. Wang, *Chin. Chem. Lett.*, 2013, **24**, 539.
- 56 A. Dhakshinamoorthy, M. Alvaro, P. Concepción, V. Fornés and H. Garcia, *Chem. Commun.*, 2012, **48**, 5443–5445.
- 57 H.-Y. Zhuo, X. Zhang, J.-X. Liang, Q. Yu, H. Xiao and J. Li, *Chem. Rev.*, 2020, **120**, 12315–12341.
- 58 J. Liu, *ChemCatChem*, 2011, **3**, 934–948.
- 59 (a) A. M. Tafesh and J. Weiguny, *Chem. Rev.*, 1996, **96**, 2035–2052; (b) V. Goyal, N. Sarki, B. Singh, A. Ray, M. Poddar, A. Bordoloi, A. Narani and K. Natte, *ACS Appl. Nano Mater.*, 2020, **3**, 11070–11079.
- 60 (a) F. Yang, C. Chi, C. Wang, Y. Wang and Y. Li, *Green Chem.*, 2016, **18**, 4254–4262; (b) V. Goyal, J. Gahtori, A. Narani, P. Gupta, A. Bordoloi and K. Natte, *J. Org. Chem.*, 2019, **84**, 15389–15398.
- 61 Z. Wei, S. Mao, F. Sun, J. Wang, B. Mei, Y. Chen, H. Li and Y. Wang, *Green Chem.*, 2018, **20**, 671–679.
- 62 Y. Sheng, X. Wang, S. Yue, G. Cheng, X. Zou and X. Lu, *ChemCatChem*, 2020, **12**, 4632–4641.
- 63 B. Zeynizadeh, Z. Shokri and M. Hasanpour Galehban, *Appl. Organomet. Chem.*, 2019, **33**, e4771.
- 64 S. Karami, B. Zeynizadeh and Z. Shokri, *Cellulose*, 2018, **25**, 3295–3305.
- 65 D. Cantillo, M. M. Moghaddam and C. O. Kappe, *J. Org. Chem.*, 2013, **78**, 4530–4542.
- 66 J. Shabir, C. Garkoti, P. Gupta, M. Sharma, S. Rani, M. Kumari and S. Mozumdar, *ACS Omega*, 2021, **6**, 1415–1425.
- 67 T. V. Thu, P. J. Ko, T. V. Nguyen, N. T. Vinh, D. M. Khai and L. T. Lu, *Appl. Organomet. Chem.*, 2017, **31**, e3781.
- 68 B. Zeynizadeh, S. Rahmani and H. Tizhoush, *Polyhedron*, 2020, **175**, 114201.
- 69 (a) J. M. García, F. C. García, F. Serna and J. L. de la Peña, *Prog. Polym. Sci.*, 2010, **35**, 623–686; (b) B. Alcaide, P. Almendros and C. Aragoncillo, *Chem. Rev.*, 2007, **107**, 4437–4492; (c) S. D. Roughley and A. M. Jordan, *J. Med. Chem.*, 2011, **54**, 3451–3479.
- 70 (a) Z. Shokri, B. Zeynizadeh and S. A. Hosseini, *J. Colloid Interface Sci.*, 2017, **485**, 99–105; (b) X. Sun, A. I. Olivos-Suarez, L. Oar-Arteta, E. Rozhko, D. Osadchii, A. Bavykina, F. Kapteijn and J. Gascon, *ChemCatChem*, 2017, **9**, 1854–1862.
- 71 (a) R. Nie, J. Wang, L. Wang, Y. Qin, P. Chen and Z. Hou, *Carbon*, 2012, **50**, 586–596; (b) M. Gilanizadeh and B. Zeynizadeh, *J. Iran. Chem. Soc.*, 2018, **15**, 2821–2837.
- 72 B. Zeynizadeh, F. M. Aminzadeh and H. Mousavi, *Green Process. Synth.*, 2019, **8**, 742–755.
- 73 B. Zeynizadeh, F. Sepehraddin and H. Mousavi, *Ind. Eng. Chem. Res.*, 2019, **58**, 16379–16388.
- 74 B. Zeynizadeh, R. Younesi and H. Mousavi, *Res. Chem. Intermed.*, 2018, **44**, 7331–7352.
- 75 B. Zeynizadeh, H. Mousavi and S. Zarrin, *J. Chin. Chem. Soc.*, 2019, **66**, 928–933.
- 76 B. Zeynizadeh, F. Mohammad Aminzadeh and H. Mousavi, *Res. Chem. Intermed.*, 2019, **45**, 3329–3357.
- 77 B. Zeynizadeh and F. Sepehraddin, *J. Organomet. Chem.*, 2018, **856**, 70–77.
- 78 G. Cheng, Y.-L. Liu, Z.-G. Wang, J.-L. Zhang, D.-H. Sun and J.-Z. Ni, *J. Mater. Chem.*, 2012, **22**, 21998–22004.
- 79 R. V. Jagadeesh, A.-E. Surkus, H. Junge, M.-M. Pohl, J. Radnik, J. Rabeah, H. Huan, V. Schünemann, A. Brückner and M. Beller, *Science*, 2013, **342**, 1073–1076.
- 80 P. L. Reddy, M. Tripathi, R. Arundhathi and D. S. Rawat, *Chem.-Asian J.*, 2017, **12**, 785–791.



- 81 D. V. Jawale, E. Gravel, C. Boudet, N. Shah, V. Geertsen, H. Li, I. N. N. Namboothiri and E. Doris, *Chem. Commun.*, 2015, **51**, 1739–1742.
- 82 M. Lauwiner, P. Rys and J. Wissmann, *Appl. Catal., A*, 1998, **172**, 141–148.
- 83 A. O. Moghanlou, M. H. Sadr, A. Bezaatpour, F. Salimi and M. Yosefi, *Mol. Catal.*, 2021, **516**, 111997.
- 84 R. Azad, A. Bezaatpour, M. Amiri, H. Eskandari, S. Nouhi, D. H. Taffa, M. Wark, R. Boukherroub and S. Szunerits, *Appl. Organomet. Chem.*, 2019, **33**, e5059.
- 85 G.-Y. Fan, L. Zhang, H.-Y. Fu, M.-L. Yuan, R.-X. Li, H. Chen and X.-J. Li, *Catal. Commun.*, 2010, **11**, 451–455.
- 86 F. Ferlin, M. Cappelletti, R. Vivani, M. Pica, O. Piermatti and L. Vaccaro, *Green Chem.*, 2019, **21**, 614–626.
- 87 S. Abdolhosseinzadeh, H. Asgharzadeh and H. Seop Kim, *Sci. Rep.*, 2015, **5**, 10160.

